



Connectional architecture of a mouse hypothalamic circuit node controlling social behavior

Liching Lo^{a,b,c,1}, Shenqin Yao^{d,1}, Dong-Wook Kim^{a,c}, Ali Cetin^d, Julie Harris^d, Hongkui Zeng^d, David J. Anderson^{a,b,c,2}, and Brandon Weissbourd^{a,b,c,2}

^aDivision of Biology and Biological Engineering, California Institute of Technology, Pasadena, CA 91125; ^bHoward Hughes Medical Institute, California Institute of Technology, Pasadena, CA 91125; ^cTianqiao and Chrissy Chen Institute for Neuroscience, California Institute of Technology, Pasadena, CA 91125; and ^dAllen Institute for Brain Science, Seattle, WA 98109

Contributed by David J. Anderson, December 12, 2018 (sent for review October 11, 2018; reviewed by Clifford B. Saper and Richard B. Simerly)

Type 1 estrogen receptor-expressing neurons in the ventrolateral subdivision of the ventromedial hypothalamus (VMHv^{Esr1}) play a causal role in the control of social behaviors, including aggression. Here we use six different viral-genetic tracing methods to systematically map the connectional architecture of VMHv^{Esr1} neurons. These data reveal a high level of input convergence and output divergence (“fan-in/fan-out”) from and to over 30 distinct brain regions, with a high degree (~90%) of bidirectionality, including both direct as well as indirect feedback. Unbiased collateralization mapping experiments indicate that VMHv^{Esr1} neurons project to multiple targets. However, we identify two anatomically distinct subpopulations with anterior vs. posterior biases in their collateralization targets. Nevertheless, these two subpopulations receive indistinguishable inputs. These studies suggest an overall system architecture in which an anatomically feed-forward sensory-to-motor processing stream is integrated with a dense, highly recurrent central processing circuit. This architecture differs from the “brain-inspired,” hierarchical feed-forward circuits used in certain types of artificial intelligence networks.

hypothalamus | aggression | social behavior | VMHv | connectivity

The hypothalamus controls an array of innate survival behaviors and associated internal motivational states, including feeding, drinking, predator defense, and social behaviors, such as mating and fighting (1, 2). It is comprised of multiple nuclei, each of which is thought to play a role in one or more behavioral functions. The connectivity of these nuclei has been extensively mapped using classic anterograde and retrograde tracing techniques (reviewed in refs. 3 and 4), revealing complex inputs to and outputs from these structures, as well as dense interconnectivity between them (5). It is increasingly clear, however, that hypothalamic nuclei are both functionally (6, 7) and cellularly (8, 9) heterogeneous. How this cellular heterogeneity maps onto connectivity, the relationship of this anatomical mapping to behavioral function, and whether there are any general principles underlying this relationship, remains poorly understood.

Genetic targeting of neuronal subpopulations and viral tools for tracing neuronal connectivity (10, 11), have provided a powerful approach to this problem in other brain systems (12–19). In the hypothalamus, viral tracers have been used to map the outputs of *Agrp*⁺ neurons in the arcuate (ARC) nucleus, which control the motivation to eat (20, 21). Although the ARC as a whole projects to ~six different regions, these studies suggested that different subsets of ARC^{AgRP} neurons project to different targets (22). Similarly, viral collateralization mapping of Galanin-expressing neurons in the medial preoptic area (MPOA) (23) have indicated that different MPOA^{GAL} neurons controlling different functions (pup-gathering, reward, etc.) project to distinct downstream targets (24). Together, these and other data (25, 26) have provided examples of hypothalamic nuclei that contain multiple functionally and connectionally distinct neuronal subpopulations. In other examples employing classic retrograde tracers, however, collateralization to dual targets has been observed (27–29).

Examples of collateralization to multiple targets, as seen in monoamine neuromodulatory systems (16, 30), are few due to limitations in the number of tracers that can be used simultaneously (31).

Type 1 estrogen receptor (*Esr1*)-expressing neurons in the ventromedial hypothalamic nucleus (VMH) control social and defensive behaviors, as well as metabolic states (6, 7, 9, 32; reviewed in refs. 33–38). Unlike the ARC^{AgRP} and the MPOA^{GAL} populations, which are primarily GABAergic (24), VMHv^{Esr1} neurons are mainly glutamatergic (39). Inputs and outputs of the VMHv and the anatomically overlapping hypothalamic attack area (HAA) (40) have been extensively mapped in rats, using conventional anterograde and retrograde tracers (41, 42). In mice, one study using a genomically integrated axonal tracer, PLAP, mapped a subset of projections from progesterone receptor-expressing VMHv neurons, which are highly overlapping with VMHv^{Esr1} neurons (32). However, inputs to and projections from VMHv^{Esr1} neurons, the extent of their collateralization, and the relationships between specific inputs and outputs have not been systematically investigated.

In this study we have used six different genetically targeted viral tracing methods to map the meso-scale connectivity of VMHv^{Esr1} neurons. Collectively, these methods reveal that these neurons

Significance

How hypothalamic cellular heterogeneity maps onto circuit connectivity, and the relationship of this anatomical mapping to behavioral function, remain poorly understood. Here we systematically map the connectivity of estrogen receptor-1-expressing neurons in the ventromedial hypothalamus (VMHv^{Esr1}), which control aggression and related social behaviors, using multiple viral-genetic tracers. Rather than a simple feed-forward sensory-to-motor processing stream, we find high convergence (fan-in) and divergence (fan-out) in VMHv^{Esr1} inputs and projections, respectively, with massive feedback. However, outputs are split into two subpopulations that project either posteriorly, to premotor structures, or anteriorly back to the amygdala and hypothalamus. This fan-in/-out system architecture is consistent with “antenna” and “broadcasting” functions for VMHv^{Esr1} neurons, with the feedback pathway possibly controlling behavioral decisions and internal state.

Author contributions: L.L., D.-W.K., D.J.A., and B.W. designed research; L.L. and D.-W.K. performed research; S.Y., A.C., J.H., and H.Z. contributed new reagents/analytic tools; L.L., D.-W.K., D.J.A., and B.W. analyzed data; and L.L., D.J.A., and B.W. wrote the paper.

Reviewers: C.B.S., Harvard Medical School, Beth Israel Deaconess Medical Center; and R.B.S., Vanderbilt University.

The authors declare no conflict of interest.

This open access article is distributed under Creative Commons Attribution-NonCommercial-NoDerivatives License 4.0 (CC BY-NC-ND).

¹L.L. and S.Y. contributed equally to this work.

²To whom correspondence may be addressed. Email: wuwei@caltech.edu or bweissb@gmail.com.

This article contains supporting information online at www.pnas.org/lookup/suppl/doi:10.1073/pnas.1817503116/-DCSupplemental.

Published online March 21, 2019.

display a high degree of convergence, divergence, and bidirectionality in their inputs and outputs, respectively. However, unlike ARC^{AgRP} (22), MPOA^{Gal} (24), and DMH^{Gal} (26) GABAergic neurons, VMHv^{Esr1} neurons collateralize to multiple downstream targets. Nevertheless, we identify Esr1⁺ neuronal subsets with broad but anatomically distinct patterns of collateralization. Together, these data suggest a system architecture in which VMHv^{Esr1} neurons receive sparse input from anteriorly located sensory structures and relay this information through two divergent processing streams: a sparse feed-forward relay targeting posterior (premotor) regions, and a highly recurrent amygdalo–hypothalamic network that may control decision-making and internal states.

Results

Extensive Bidirectional Connectivity of Projections and Inputs of VMHv^{Esr1} Neurons. Inputs to and projections from the VMHv^{Esr1} have been mapped in several studies using classic techniques in rodents (e.g., CTb and PHAL) (40–48). However, these techniques are unable to distinguish genetically defined cell populations within the VMHv, which is heterogeneous (6, 9). Furthermore, with a few exceptions (49, 50) most studies report on a single type of tracing method (e.g., anterograde or retrograde), making it difficult to directly compare results across publications. To systematically map the inputs and outputs of VMHv^{Esr1} neurons, we used *Esr1-Cre* knockin mice (7), together with Cre-dependent AAV-based anterograde (15) and modified monosynaptic rabies-based retrograde (10, 11) viruses (*Methods*), stereotaxically injected into VMHv. Results were analyzed using serial two-photon tomography (Tissue-Cyte) (51) at 100- μ m z-intervals with 0.35- μ m x–y resolution. Esr1⁺ neurons form a continuous population that extends from the VMHv into the neighboring Tuberal nucleus (TU). Across experiments described in this study, the majority (~77%) of starter cells were located in these two regions combined, a population referred to hereafter as VMHv^{Esr1}.

Anterograde (nontransneuronal) tracing using Cre-dependent adeno-associated virus 1 (AAV1)-GFP (15) revealed projections of VMHv^{Esr1} neurons to over 60 target regions (Fig. 1A–E and *SI Appendix*, Fig. S1A; see *SI Appendix*, Table S1 for brain region abbreviations). Most of these targets were previously described in nongenetically based *Phasolus vulgaris*-leucoagglutinin (PHAL) tracing studies (40, 42), with the exception of a few weak projections (*SI Appendix*, Table S2). Quantitative analysis of relative projection strength to each of 30 principal targets, using fluorescence pixel intensity, revealed strong projections within the hypothalamus, including the MPOA, paraventricular nucleus (PVN), anterior hypothalamus nucleus (AHN), dorsomedial hypothalamus (DMH) and ventral premammillary (PMv), and the extended amygdala [including the bed nucleus of the stria terminalis (BNST)], as well as posterior projections to the midbrain and brainstem, including the periaqueductal gray (PAG) dorsomedial (dm), PAG ventrolateral (vl), median raphe nucleus (MRN), and ventral tegmental area (VTA) (Fig. 1K; see color code for their position relative to VMHv). A comparison of projections in males and females ($n = 2$ each) did not reveal consistent differences (*SI Appendix*, Table S3) (but see ref. 32).

To map presynaptic inputs specifically to the VMHv^{Esr1} population, we performed Cre-dependent monosynaptic, retrograde, transneuronal tracing (52–54), using N2c rabies virus encoding a nuclear GFP reporter (*Methods* and Fig. 1F). Sections were analyzed using brain-wide serial two-photon tomography, as above, and the number of cells in each region was manually quantified. We observed detectable retrograde labeling in 63 different structures, all but 7 of which were identified in an earlier nongenetically based retrograde tracing study from VMHv in the rat using CTb (41) (*SI Appendix*, Table S4). Notably, the vast majority of inputs to VMHv^{Esr1} neurons are located subcortically, particularly in the hypothalamus and extended amygdala. However, we also detected significant input from the ventral

subiculum (SUBv), as well as from the medial prefrontal cortex (mPFC) (Fig. 1F–J and L and *SI Appendix*, Fig. S1B).

Strikingly, with a few notable exceptions (see below), monosynaptic retrograde labeling was found in the majority of structures to which VMHv^{Esr1} neurons also project (Fig. 1K–P and *SI Appendix*, Fig. S1A and B). Because many of these input regions themselves contain Esr1⁺ neurons, we were concerned that the Cre-dependent, transcomplementing AAV encoding TVA-2A-rabies glycoprotein (RG) injected into the VMHv might infect axons from these VMH-extrinsic Esr1⁺ inputs, subsequently allowing for primary infection of those terminals by the EnvA-pseudotyped rabies virus (and therefore GFP expression in their cell bodies, creating a false impression of retrograde monosynaptic labeling). To control for this, a separate cohort of mice were injected with a control Cre-dependent AAV encoding only TVA, and not RG. With the exception of local expression of GFP in VMHv, expression of the rabies-encoded nuclear GFP marker was not detected in input regions (*SI Appendix*, Fig. S1C and D), indicating that the VMH-extrinsic GFP expression observed in the transcomplementing animals was dependent on the expression of the transcomplementing RG protein, and therefore indeed reflected monosynaptic, retrograde tracing.

To compare quantitatively the relative strength of VMHv^{Esr1} projections vs. inputs for each structure, we determined the ratio, plotted on a log scale, of the normalized input strength to the normalized output strength for 30 different regions (Fig. 1N and *SI Appendix*, Tables S5 and S6). Thus, the closer the log-ratio value to 0, the higher the likelihood that the normalized strength of inputs from a given region was equal to the normalized projection (output) strength to that region (e.g., MPOA, ~9% of total projections and ~9% of total inputs; ratio = 1; log ratio = 0) (Fig. 1K–N). Approximately 40% (12 of 30) of the regions analyzed in this way had log-ratio values between +0.3 and –0.3 (Fig. 1N), indicating relatively balanced (less than twofold different) bidirectional connectivity. In contrast, only 20% (6 of 30) of the regions sampled had an input bias (ratio > 3, log ratio > 0.48), while a similar percentage showed an output bias (ratio < 0.33, log ratio < –0.48). Most notable among input-biased areas was the SUBv, which contributed ~7% of all inputs but which received almost no projections, while among output-biased areas the PAG received ~5% of all outputs but <1% of all inputs (Fig. 1K–N and P).

To analyze these data further, we ranked input-biased structures and output-biased structures based on the ratio of the normalized inputs/outputs for each structure (*SI Appendix*, Tables S6 and S7). Interestingly, input-biased structures were distributed primarily anterior to, or in the same anterior–posterior (A–P) region as, the VMHv (*SI Appendix*, Table S7, columns 2 and 3), and included sensory regions [taenia tecta dorsal (TTd), medial amygdala (MeA), BNST principal (pr)], while projection-biased structures were distributed more posteriorly and included most of the midbrain premotor targets (e.g., PAGdm, PAGvl, MRN) (*SI Appendix*, Table S7, columns 5 and 6). The average distance from Bregma was significantly different ($P < 0.03$) for input-biased vs. output-biased targets (*SI Appendix*, Table S7, columns 4, 7, and 10), with the former containing the most anterior [mPFC, TTd, lateral septal neuron (LS)] and the latter the most posterior (PAGdm, PAGvl, MRN) targets. To further analyze unbiased regions that have the greatest combination of both connectivity strength and bidirectionality, we plotted the sum of each region's normalized inputs and projections (strength) minus the absolute value of the difference between input and projection (bias) (Fig. 1O); thus high strength and high bidirectionality gave the highest relative values. These strongly bidirectionally connected regions included most intrahypothalamic and extended amygdala targets (e.g., MPOA, AHN, BNST) (Fig. 1O and P and *SI Appendix*, Table S7, columns 8, 9, 11, and 12).

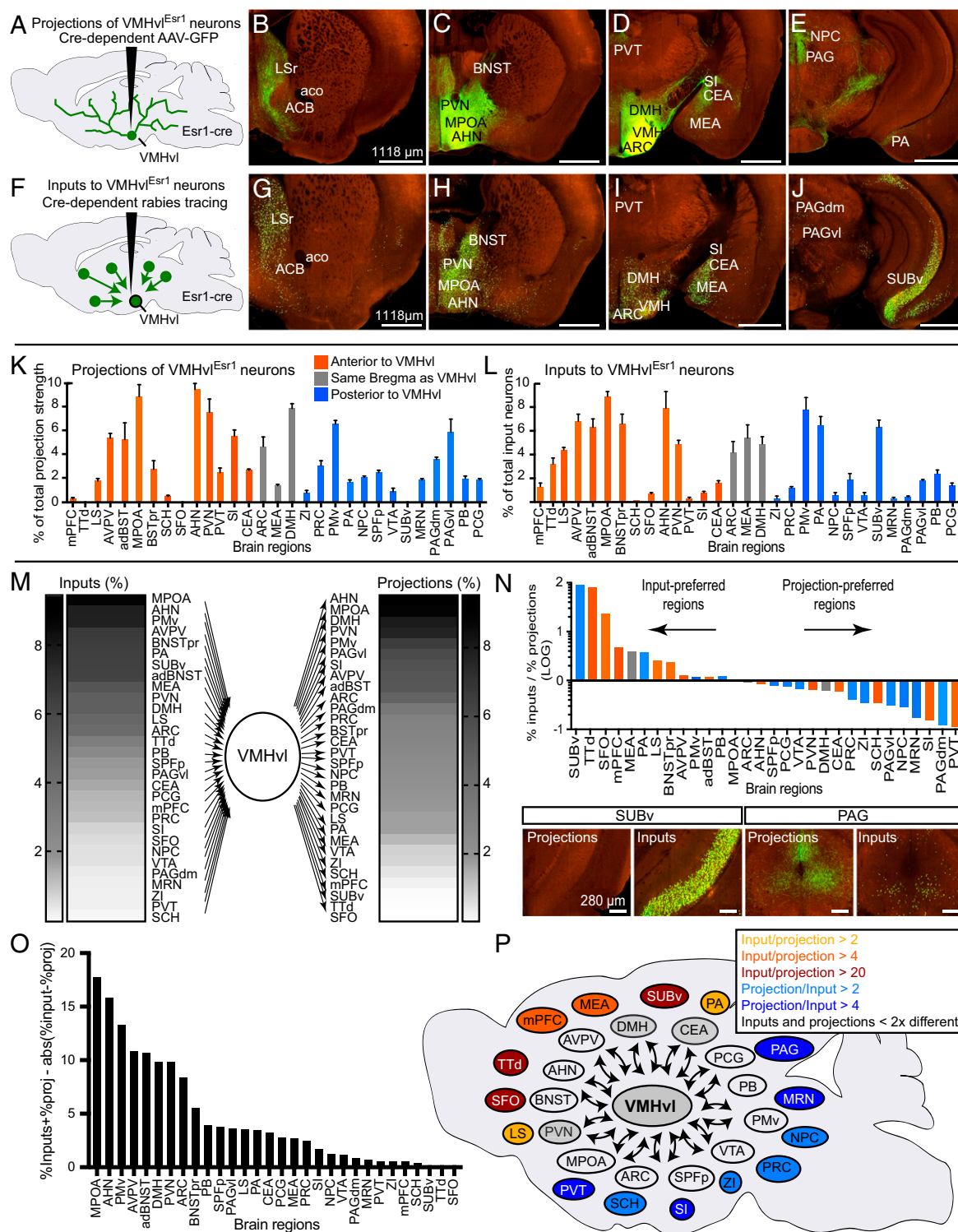


Fig. 1. Inputs to and outputs from VMHv1^{Esr1} neurons. (A–E) Projections of VMHv1^{Esr1} neurons. (A) Experimental schematic. (B–E) Representative images of AAV-GFP labeled projections (Image credit: Allen Institute). (F–J) Inputs to VMHv1^{Esr1} neurons revealed by monosynaptic rabies tracing. (F) Experimental schematic. (G–J) Representative images of rabies-GFP labeled inputs. (K) Proportion of total projections in each of 30 areas ($n = 3$). All bar graphs with error bars represent means + SEMs. Color code corresponds to anterior (orange), posterior (blue), or similar (gray) A–P location relative to the VMHv1; regions arranged from anterior (Left) to posterior (Right). (L) Proportion of total inputs, shown in F–J, graphed as in K. CEA, central amygdalar nucleus; NPC, nucleus of the posterior commissure; PB, parabrachial nucleus; PCG, pontine central gray. (M) Schematic summarizing the percent of total inputs (Left) or outputs (Right). (N) Relative bias toward inputs or projection strength, calculated by dividing normalized input strength (L) by normalized projection strength (F). Color code is as in K. (Lower) Example structures with strong input (SUBv) or projection (PAG) bias. (O) Histogram for visualizing estimated strength and balance of bidirectional connectivity, calculated by subtracting the absolute value of the difference between normalized input strength (L) and normalized projection strength (F) from their sum. (P) Summary schematic; bias of regions toward input or output shown using heat-map coloration. See *SI Appendix, Fig. S1* for control experiments, micrographs of input and output regions, and additional data. See *SI Appendix, Table S1* for list of abbreviations and *SI Appendix, Tables S5–S7* for rank-ordered lists and relative positions of regions.

We next asked whether different input regions send predominantly glutamatergic or GABAergic projections to the VMHvl. To do this, we used a method we call input-neurotransmitter-selective retrograde tracing (INSERT) by injecting retrograde herpes simplex virus (HSV) harboring a Cre-dependent mCherry reporter into the VMHvl of either vGlut2-cre or vGAT-cre mice. Retrograde transport of the virus and recombination revealed the brain-wide distribution of vGlut2⁺ or vGAT⁺ neurons that project to the VMHvl (although not to *Esr1*⁺ neurons specifically) (*SI Appendix, Fig. S1E*). These experiments indicated that most (63%) of the VMHvl input regions are either primarily glutamatergic or GABAergic, but not both (*SI Appendix, Fig. S1 F-H*). The posterior amygdala (PA), precommissural nucleus (PRC), subparafascicular nucleus parvicellular part (SPFP), and PMv provide the majority of predominantly glutamatergic input, while the BNSTpr, MPOA, AHN, and DMH provide the majority of predominantly GABAergic input (*SI Appendix, Fig. S1 F-H*). Among those input regions containing both glutamatergic and GABAergic neurons, most send inputs of both types to the VMHvl. MPOA, anteroventral periventricular (AVPV), and ARC send equal proportions of glutamatergic and GABAergic inputs, while other regions show either a strong bias to GABAergic [BNSTpr and anterior TU] or to glutamatergic inputs [mPFC, MeAv, posterior amygdalar nucleus (pPA), SUBv, and PAGdm] (*SI Appendix, Fig. S1 F-H*).

Higher-Order Projections from VMHvl Reveal Indirect Feedback to Select Presynaptic Inputs. To identify second and higher-order projections of VMHvl^{Esr1} neurons, we performed poly-synaptic, anterograde, transneuronal tracing using a Cre-dependent H129 virus (Fig. 2A) (55). Survival times were limited to ~40–50 h to restrict viral movement to an estimated 2 ± 1 synapses (55, 56). As expected, postsynaptic labeling was seen in most of the structures to which VMHvl^{Esr1} neurons project directly, including the PAG, MPOA, ARC, and BNSTpr (Fig. 2B–G). Strikingly, however, strong labeling was also observed in several areas to which VMHvl^{Esr1} neurons were not seen to directly project (Fig. 2H and I), but from which they receive strong input; these included the SUBv, TTd, and subfornical organ (SFO) (Fig. 2I and *SI Appendix, Fig. S2 E–G*). These observations are suggestive of poly-synaptic feedback from the VMHvl to these input structures (Fig. 2J and *SI Appendix, Fig. S2N*). [However, we cannot formally exclude that this reflects input-specific retrograde labeling by the H129 virus (see discussion in refs. 55 and 57).] We also identified indirect feedback to the suprachiasmatic nucleus (SCH) (*SI Appendix, Fig. S2 A–C*), which has recently been shown to mediate circadian control of aggression, via indirect projections to VMHvl^{Esr1} neurons (58). Finally, although VMHvl^{Esr1} neurons exhibit very weak direct projections to the mPFC, (Fig. 1K), we observed clear anterograde transsynaptic labeling of cells in the prelimbic area (PL) and infralimbic area (ILA) (Fig. 2B). To exclude the possibility that the labeling of strong input regions, such as the SUBv, was due to retrograde infection of *Esr1*⁺ axon terminals originating in those structures (55), we injected a retrograde HSV (not HSV129) expressing Cre-dependent mCherry into the VMHvl of *Esr1-Cre* mice, as described in the INSERT tracing above. In these experiments we saw little to no labeling in the SUBv, TTd, and SFO (*SI Appendix, Fig. S2 I–L*).

VMHvl^{Esr1} Neurons Show Extensive Collateralization. The population-level projection mapping described above (Fig. 1) did not distinguish whether the multiple projection targets of VMHvl^{Esr1} neurons (Fig. 1K and *SI Appendix, Fig. S1A*) reflect collateralization by individual neurons, or rather a mixed population, each of which has relatively restricted, specific projections. To investigate this issue, we performed collateralization mapping of VMHvl^{Esr1} neurons, using a modification of a previously described method (16). In this approach, a Cre-dependent, retrogradely transported HSV

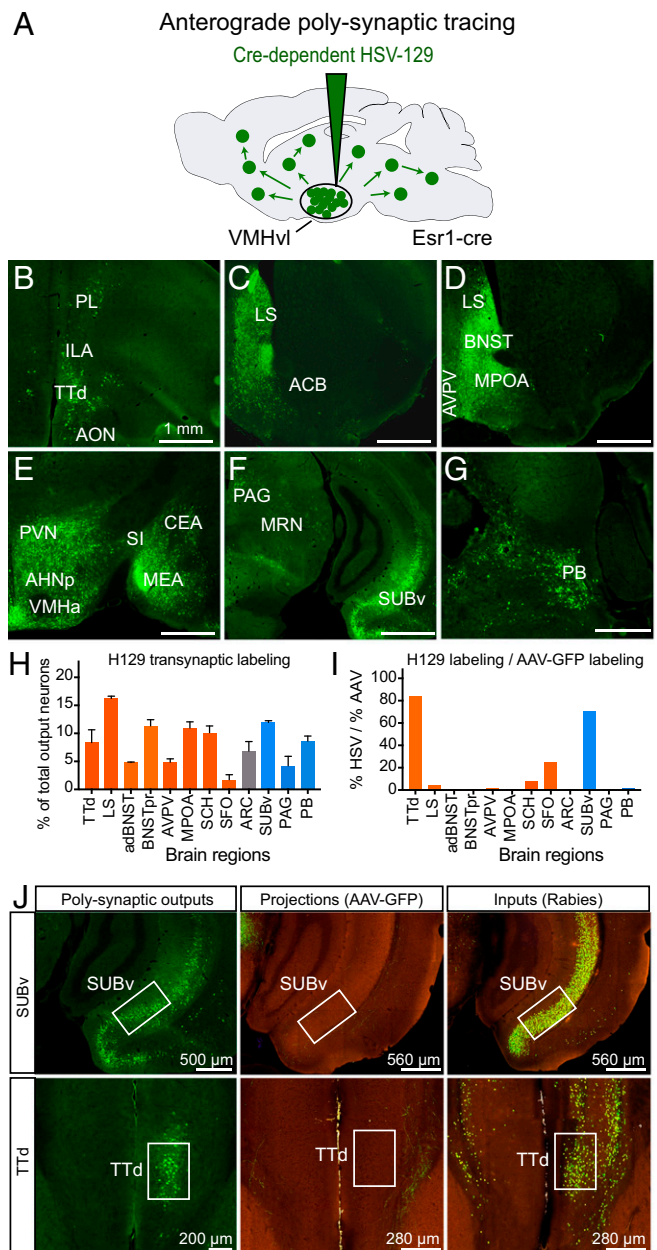


Fig. 2. Indirect feedback loops revealed by anterograde transsynaptic tracing. (A) Schematic of experiment showing anterograde, poly-transsynaptic tracing via injection of H129 Δ TK-TT virus into the VMHvl of *Esr1-Cre* mice. (B–G) Representative images of anterograde transsynaptic tracing from VMHvl^{Esr1} neurons. (H) Quantification showing the percent of total H129 Δ TK-TT labeled output neurons in 12 regions (mean + SEM, $n = 2$). Bar color code reflects whether the region is located anterior (orange) or posterior (blue) to the VMHvl. (I) Ratio of H129 Δ TK-TT labeling to AAV-GFP projections in the corresponding regions. AAV-GFP-based projections for the same 12 selected regions were extracted from Fig. 1F and normalized to 100% for comparison with data in H. (J) Representative images comparing HSV-labeled polysynaptic outputs (Left), AAV-GFP-based projections (Center), and rabies-GFP labeled inputs (Right) in the SUBv and TTd. See *SI Appendix, Fig. S2* for additional data and analysis.

encoding FLPo recombinase is injected into one projection target of *Esr1*⁺ neurons, while a FLPo-dependent AAV encoding GFP is injected into the VMHvl of *Esr1-Cre* mice (Fig. 3A and B). This intersectional strategy results in GFP expression specifically in VMHvl^{Esr1} neurons that project to the target region-of-interest. Because GFP is freely diffusible, it fills each neuron,

either the MPOA or dmPAG, there were important quantitative differences as well (Fig. 3 C and D). VMHvl^{Esr1} neurons that project to the MPOA, which is located anterior to the VMH, collateralized significantly more strongly to other anteriorly located targets, while VMHvl^{Esr1} neurons projecting to the dmPAG, which is located posterior to the VMH, collateralized more strongly to other posteriorly located targets (Fig. 3 C and D). Two-way ANOVA revealed a strong interaction between the HSV^{LS1L-FLPo} injection site (MPOA vs. PAG) and the distribution of labeling in collateral projection domains (Fig. 3C) ($P = 0.0001$, MPOA and PAG omitted from the analysis). We also observed a strong correlation between the A–P location of different target regions, and their relative collateralization strength between MPOA- and PAG-projecting populations (Fig. 3D) ($R^2 = 0.47$, $P < 0.001$).

A similar bias was observed when comparing the collateral projections of VMHvl^{Esr1} neurons back-labeled from the LSv, another region anterior to the VMH, to those back-labeled from the PAG (SI Appendix, Fig. S3 A–C), while comparison of collaterals of VMHvl^{Esr1} neurons back-labeled from the LSv and MPOA revealed no significant differences (SI Appendix, Fig. S3 D and E). Thus, although VMHvl^{Esr1} neurons as a whole collateralize extensively, we find evidence of subpopulations that project to combinations of target regions located either anterior or posterior to the VMH itself (Fig. 3 C and D). However, within each of these two subpopulations, these data do not distinguish between a range of possible connectivity patterns, consistent with the results, which may include some neurons with projections to a single target (Fig. 3E).

Projection-Defined Subpopulations of VMHvl^{Esr1} Neurons Differ in Soma Location and Size. Our finding of projection-biased subpopulations led us to analyze characteristics of these Esr1⁺ subpopulations in the VMHvl, particularly as previous studies have described differences in cell morphology in the VMH (59–61). Interestingly, we observed that the cell somata of the anteriorly vs. posteriorly projecting VMHvl^{Esr1} neurons described above exhibit a distinct and complementary distribution along the A–P axis: anteriorly projecting cells (injected with retrograde HSV^{LS1L-FLPo} virus in the MPOA or LSv) were located in the more posterior domain of the VMHvl (–1.58 to –2.06 mm from Bregma), while posteriorly projecting cells (injected with retrograde HSV^{LS1L-FLPo} virus in the PAG) were located in the more anterior region of the VMHvl (–1.34 to –1.82 mm from Bregma) (Fig. 4 A and B and SI Appendix, Fig. S3F). This between-animal comparison was confirmed by a within-animal comparison using dual injections of HSV-LS1L-mCherry into the MPOA and of HSV-LS1L-eYFP into the dmPAG of *Esr1-Cre* mice (Fig. 4 C and D). Serial sectioning revealed opposing gradients of dmPAG- and MPOA-projecting neurons along the A–P axis, with the former peaking more anteriorly (–1.34 to –1.46 mm from Bregma) and the latter peaking more posteriorly (–1.7 mm from Bregma) (Fig. 4D). Moreover, within individual sections containing both back-labeled populations, dmPAG-projecting and MPOA-projecting VMHvl^{Esr1} neurons were largely non-overlapping [Fig. 4C, (“overlay”) and Fig. 4D] (overlap less than expected based on random distribution, $P < 0.01$).

Further analysis indicated that the average somata diameters of the MPOA- and PAG-projecting neurons were significantly different, with the latter being almost 60% larger than the former ($964 \pm 65 \mu\text{m}^3$ vs. $609 \pm 46 \mu\text{m}^3$, $P < 0.001$) (Fig. 4 E and F). In addition, the average fiber mass per cell (an indirect measure of branching within VMHvl) was significantly larger for PAG-projecting than for MPOA-projecting Esr1⁺ neurons ($P < 0.01$) (Fig. 4 E and G). Taken together, these data reveal significant differences in cell body distribution (along the A–P axis of the 3 VMHvl), cell somata size, and local branching for anteriorly vs. posteriorly projecting Esr1⁺ neurons in the VMHvl, as well as minimal overlap among

these cells at A–P positions where both are located, suggesting that they represent distinct subpopulations of Esr1⁺ neurons.

Projection-Biased Subsets of Esr1⁺ Neurons Receive Similar Inputs.

The existence of different subpopulations of Esr1⁺ neurons exhibiting anterior or posterior biases in their collateralization patterns raised the question of whether these subpopulations differ in their inputs. To address this question directly, we performed a modification of the TRIO (tracing the relationship between input and output) method (16), in which monosynaptic, retrograde, transsynaptic tracing is performed on subsets of Esr1⁺ neurons, as defined by their projections. In this experiment, *Esr1-Cre* mice were injected in either the MPOA or PAG with a Cre-dependent HSV-LS1L-FLPo virus to express FLPo in Esr1⁺ neurons with anteriorly vs. posteriorly biased projections, respectively; these same mice were injected in the VMHvl with FLPo-dependent AAVs encoding TVA-mCherry and RG for rabies tracing. Following 3 wk of incubation, the animals were additionally injected in the VMHvl with EnvA-pseudotyped rabies^{ARG} expressing GFP (Fig. 5 A and B). Following a further 6 d of incubation, animals were killed and the pattern of GFP labeling quantified.

Interestingly, despite the differences in cell body location, size, and the separation of projection targets between these two VMHvl^{Esr1} populations, retrogradely labeled input cells could be found in similar structures following rabies tracing from each of these two VMH populations (Fig. 5 A–D). There were no statistically significant differences in the proportion of back-labeled cells in each of 29 input areas analyzed, and no significant interaction between projection target and the proportion of labeling in input regions (two-way ANOVA, $P < 0.96$) (Fig. 5C). This does not exclude the existence of subtle but biologically significant specificity that is obscured by the multiple sources of variability in this four-virus experiment.

To confirm that rabies labeling was in fact generated from the distinct projection populations of VMHvl^{Esr1} neurons described above (Fig. 4), we quantified the distribution of viral back-labeled (i.e., HSV-LS1L-FLPo-expressing) and rabies-infected starter cells (Rabies-GFP⁺, TVA-mCherry⁺), along the A–P axis of the VMHvl, in mice where rabies tracing was performed from PAG–back-labeled vs. MPOA–back-labeled cells. Similar opposing gradients of cell somata distributions were observed, as in the collateralization-mapping experiments (Fig. 4A), with the distribution of MPOA–back-labeled cells shifted posteriorly relative to that of PAG–back-labeled cells (SI Appendix, Fig. S4). Taken together, these data indicate that MPOA-projecting (posteriorly located, anteriorly collateralizing) vs. PAG-projecting (anteriorly located, posteriorly collateralizing) VMHvl^{Esr1} neurons receive a similar combination of presynaptic inputs (Fig. 5D).

Discussion

Esr1⁺ neurons in VMHvl control social investigation, mounting, and fighting, as well as internal states related to these behaviors. To investigate the anatomical input–output logic of this brain region and to provide a foundation for understanding this functional diversity, we have carried out systematic mapping of inputs to and outputs from these neurons using six different types of viral-genetic tracing systems: (i) anterograde projection mapping; (ii) retrograde, monosynaptic, transneuronal tracing; (iii) INSERT; (iv) anterograde, polysynaptic, transneuronal tracing; (v) collateralization mapping; and (vi) mapping the relationship between inputs and projection patterns. This combination of tracing techniques has afforded a brain-wide overview of the collateralization patterns of Esr1⁺ neuronal projections, and of the input–output logic of these neurons as defined by the intersection of gene expression and projection pattern.

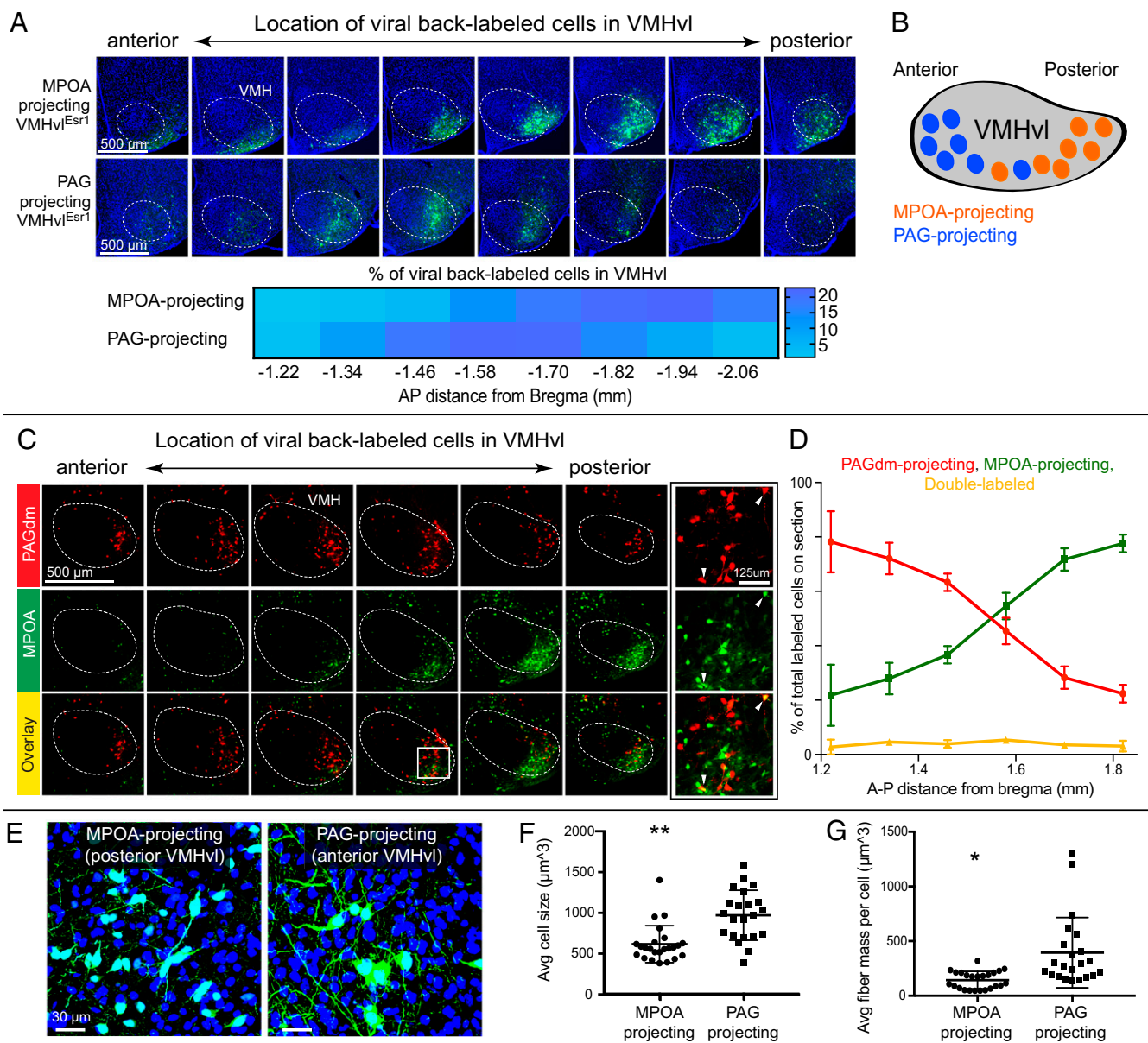


Fig. 4. Distinct characteristics of VMHv1^{Esr1} neurons that project to the MPOA vs. PAG. (A) Representative images (Upper) and heatmap (Lower) showing the distribution along the A-P axis of VMHv1^{Esr1} neurons back-labeled with Cre-dependent HSV that project to the MPOA (Upper) versus the PAG (Lower) ($n = 2/\text{each}$). (B) Schematic illustrating the complementary position of back-labeled neurons in the VMHv1. (C) Representative images of coronal sections showing the distribution of neurons in the VMHv1 that were back-labeled via injection of Cre-dependent HSV-mCherry into the PAG and Cre-dependent HSV-EYFP into the MPOA of *Esr1-Cre* mice. High-magnification images of labeled VMHv1 neurons shown in the rightmost panels correspond to the boxed region in the Bottom-Center micrograph. Arrowheads point to double-labeled cells. (D) Quantification of the distribution of back-labeled cells in the VMHv1 (mean \pm SEM, $n = 3$). (E) Representative confocal images of VMHv1 *Esr1* cell bodies back-labeled using Cre-dependent HSV from either the MPOA (Left) or PAG (Right). (F) Cell volume of MPOA- vs. PAG-projecting VMHv1^{Esr1} neurons back-labeled as in E (mean \pm SEM, $n = 4$ mice/each; total neurons: $n = 997$ from MPOA and $n = 522$ from PAG, $**P < 0.001$). (G) Average fiber mass for MPOA- vs. PAG- projecting VMHv1^{Esr1} neurons back-labeled as in E (mean \pm SEM, $n = 4$ mice/each, $*P < 0.01$).

Fan-In/Fan-Out Organization and Bidirectionality of VMHv1 Inputs and Outputs. Previous studies of VMH connectivity using non-genetically targeted tracers have demonstrated that this nucleus receives inputs from and projects to diverse structures (41, 42). The present studies confirm and extend these and other classic studies of VMHv1 connectivity (40, 45) in several important ways. First, they demonstrate a similarly high degree of input convergence and of output divergence for specifically the *Esr1*⁺ subset of VMHv1 neurons. It is somewhat surprising that the overall pattern of inputs and outputs is so similar for *Esr1*-restricted vs. nongenetically restricted labeling of VMHv1 neurons, given that the

former only represent $\sim 40\%$ of the latter (7). However, the VMHv1^{Esr1} population is itself heterogeneous (9), and our data reveal heterogeneity in collateralization patterns within this population. Furthermore, some of the inputs and projections may specifically map to *Esr1*⁺ neurons in the adjacent TU region due to spillover of injected viruses. Projection mapping of more specific VMHv1^{Esr1} neurons defined by intersectional and activity-dependent genetic labeling methods (50) may help to resolve this issue.

Second, VMHv1^{Esr1} neurons demonstrate a high degree of bidirectional connectivity between their inputs and outputs: of 30 input regions analyzed, 90% also receive feedback projections

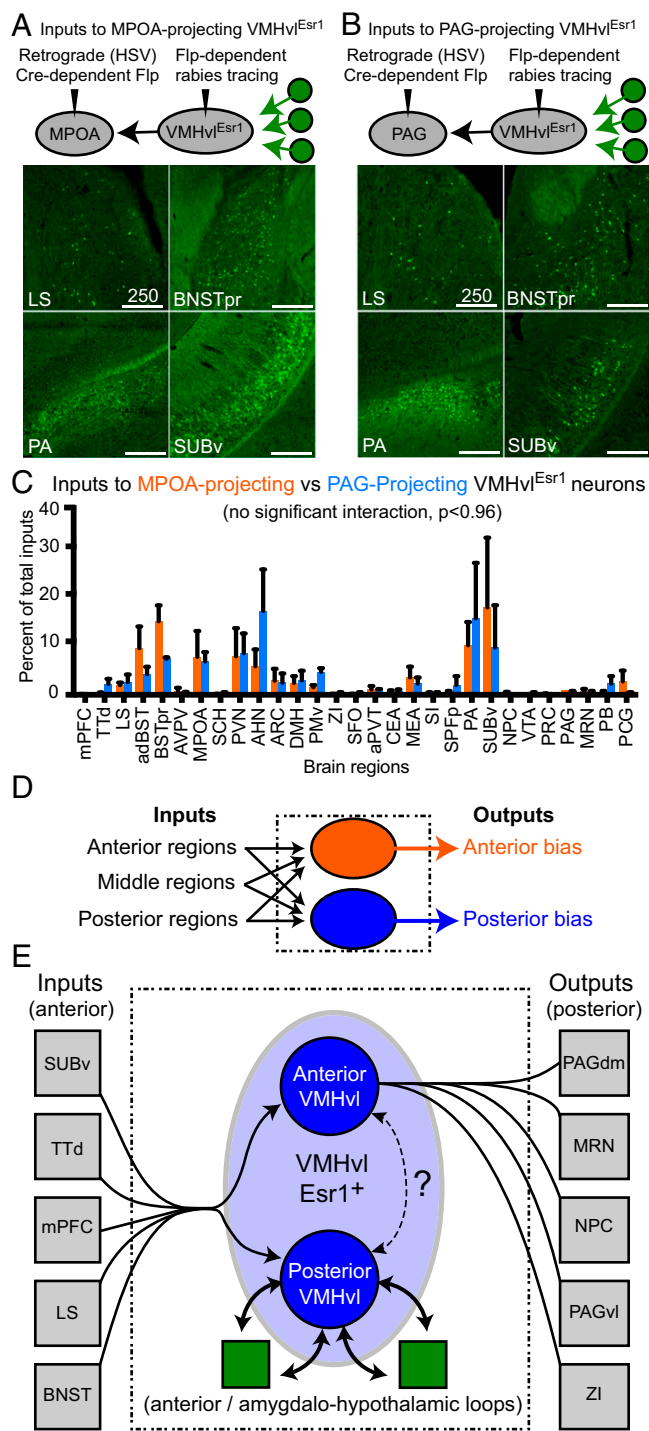


Fig. 5. Projection-biased VMHvl^{Esr1} subpopulations receive similar inputs. (A) Tracing inputs to VMHvl^{Esr1} neurons that project to the MPOA. Schematic of experiment shown (Upper) with representative images of coronal sections showing rabies labeled inputs below. (B) Tracing inputs to VMHvl^{Esr1} neurons that project to the PAG. Schematic of experiment shown (Upper) with representative images of coronal sections showing rabies labeled inputs below. (Scale bars, 250 μ m in A and B.) (C) Quantification of the proportion of total inputs from 29 regions (mean \pm SEM, $n = 2$ /each). There is no significant interaction observed by two-way ANOVA ($P < 0.96$) or differences between specific regions. See *SI Appendix, Fig. S4* for distribution of soma locations for MPOA vs. PAG back-labeled cells. (D) Schematic illustrating results of collateralization mapping in which subpopulations of VMHvl^{Esr1} neurons collateralize to distinct combinations of anterior or posterior targets yet receive the same inputs. (E) Schematic showing overall summary of VMHvl^{Esr1} circuit architecture.

from Esr1⁺ neurons in VMHvl, and the remaining 10% receive indirect, polysynaptic feedback projections. Such a direct comparison would be difficult to make based on earlier studies, which typically examined either inputs or outputs, but not both. However, it is unknown how the different viral tracing techniques used in this comparison (i.e., AAV-GFP vs. rabies) relate to functional synaptic connectivity. Nevertheless, the data reveal that the vast majority of the inputs and outputs of VMHvl^{Esr1} neurons are located subcortically, particularly in the hypothalamus and extended amygdala, and that most of these connections are bidirectional. However, there is input from the SUBv (hippocampus), as well as from the mPFC. Interestingly, the ventral hippocampus does not receive direct feedback from the VMHvl, although we observe an indirect recurrent projection to the SUBv.

Third, using a two-virus collateralization mapping technique not previously applied to the VMH, we find that Esr1⁺ neurons collateralize to multiple (≥ 5) targets (fan-out). These findings contrast with previous viral-based unbiased collateralization mapping studies of hypothalamic populations involved in feeding or parenting behavior that reported mainly one-to-one projections (22, 24). Fourth, and most important, we find that VMHvl contains at least two subpopulations of Esr1⁺ neurons with different cell body sizes, local branching patterns, and differential soma distributions along the A-P axis, which exhibit distinct anterior vs. posterior biases in their pattern of collateralization. Nevertheless, these two projection-defined, Esr1⁺ subpopulations of VMHvl neurons receive a similar distribution of fan-in inputs from the same anatomical regions, as assessed using the TRIO method (Fig. 5D).

VMHvl^{Esr1} Neurons Collateralize Broadly Yet Specifically. Classic studies of collateralization in the hypothalamus typically have employed injection of different retrograde tracers into pre-selected target regions, and reported varying degrees of colabeling in the nuclei examined, ranging from a few percent to more than half (27–29, 31, 62–65). However, this strategy suffers from a number of limitations, including preselection of targets and the ability to examine only two to three targets at a time. To date, systematic and unbiased collateralization mapping has been performed for only a few genetically defined hypothalamic populations using viral techniques similar to those applied here: projections of ARC^{Agrp} neurons, which control hunger, exhibit little collateralization and a high degree of target specificity, suggesting a one-to-one organization (22). Similar observations have recently been reported for MPOA^{Gal} neurons involved in parenting behavior (24). Interestingly, both of those populations are GABAergic.

Here we have shown that VMHvl^{Esr1} neurons, which are largely glutamatergic, exhibit substantial collateralization in their projections. While our population data demonstrate that at least some VMHvl^{Esr1} neurons collateralize to multiple targets, they do not prove that individual neurons collateralize to all five to six targets, nor do they exclude that some neurons may project exclusively to single targets (Fig. 3E). Whole-brain mapping of single VMHvl^{Esr1} neuronal projections in sparsely labeled preparations, and bar-coded viral labeling and terminal sequencing (66) will be necessary to resolve this issue. Collateralization could, in principle, impose temporal synchrony on targets of VMHvl^{Esr1} neurons and coordinate their activity. Given this collateralization, assigning specific functions to individual projections (e.g., by optogenetic terminal stimulation) (22) will be technically challenging, due to back-propagation and collateral redistribution of action potentials from optogenetically stimulated terminals.

Although VMHvl Esr1⁺ neurons project to multiple targets, we nevertheless observed that subpopulations of VMHvl^{Esr1} neurons exhibit biases in their collateralization to different combinations of target regions. One pattern is biased toward more posterior structures, while the other is biased toward anterior structures.

The neurons exhibiting these collateralization biases, moreover, exhibit differences in A–P location within VMHvl, differences in cell body size and degree of local branching, and are largely nonoverlapping in dual-labeling experiments. This suggests that they may represent distinct cell classes or cell types, possibly corresponding to those described using classic Golgi staining (67). Clarification of this issue could be achieved using single-cell RNA sequencing in combination with retrograde labeling, FISH, and quantitative analysis of cell morphology.

Overall System Architecture of VMHvl^{Esr1} Neurons. Although the results presented here indicate that VMHvl^{Esr1} neurons exhibit a high degree of connectional complexity, some broad features of system architecture can be extracted (Fig. 5E). First, despite the high level of bidirectional connectivity (Fig. 1), there are a few areas that are strongly biased inputs to, or outputs from, these neurons. The former include TTD, an olfactory processing area; the SFO, an interoceptive circumferential organ; the ventral hippocampus (SUBv), and the mPFC. These areas tend to be located anterior to the VMH. The latter include the PAG and MRN, which are premotor regions located posterior to the VMH. In contrast, VMHvl^{Esr1} neurons exhibit the strongest level of bidirectional connectivity with other hypothalamic nuclei (MPOA, AHN, ARC, DMH) and extended amygdalar (MeA, BNSTpr) regions, many of which are located at similar A–P levels as the VMH (Fig. 1P).

This pattern of connectivity suggests that there is a sparse A–P flow of information through the VMH, from sensory/cognitive to premotor regions, respectively, with a network of highly recurrent connectivity interposed between these input and output processing streams (Fig. 5E). The high degree of feedback between VMHvl^{Esr1} neurons and the surrounding amygdalo-hypothalamic structures is suggestive of an analog controller. Given the limited set of premotor target structures of VMHvl^{Esr1} neurons, such a system may function as a circuit dedicated to the finely tuned, dynamic control of a small set of social behaviors, including aggression, social investigation, and mounting, and their associated internal states.

This overall system architecture provides an attractive a posteriori rationalization for the two divergent subpopulations of VMHvl^{Esr1} neurons identified here. On the one hand, the posteriorly projecting population conveys output from the nucleus to premotor structures that control behavior (Fig. 5E, Right). On the other hand, the anteriorly projecting population provides feedback to hypothalamic and amygdalar circuitry (Fig. 5E, Center). This circuitry may control internal state, competition with opponent behaviors, or other aspects of behavioral decision-making. Such an organization raises the question of how these two VMHvl^{Esr1} populations communicate with, and are coordinated with, each other. Communication could involve local interneurons within the VMHvl (Fig. 5E, dashed arrows), while coordination could be achieved through the observed parallelization of inputs to both subpopulations. While clearly speculative, this inferred system architecture makes a number of predictions that can be explored in future studies.

Open Questions. The methods used in this study leave open several important questions. First, we do not yet know the degree of neuronal subtype diversity among VMHvl^{Esr1} neurons, and its relationship to overall VMHvl connectional architecture. It is already clear from recently published work that the VMHvl contains subpopulations of neurons with social behavior functions distinct from those involved in aggression (6, 7, 9, 50). This microheterogeneity leaves open the possibility that simplifying features and principles will emerge when the connectivity and function of these more specific subpopulations is eventually mapped.

Second, we do not know the cellular identities of the various inputs and outputs identified in this study. We have identified

both glutamatergic and GABAergic neurons that project to VMHvl, but which of these cells are monosynaptic inputs to *Esr1*⁺ neurons, and how these specific inputs relate to downstream targets, remains unknown. Similarly, we do not know the precise combinations of downstream regions targeted by individual VMHvl^{Esr1} neurons, or the identities of the cells that are postsynaptic to these projections. The latter is important because a given bidirectional projection could mediate either net positive- or net negative-feedback, depending on whether the immediate postsynaptic targets are, for example, excitatory or local inhibitory neurons, respectively. Connectivity mapping strategies involving transsynaptic tracing, single-cell RNA sequencing, and bar-coding (66) may help to resolve these issues.

Finally, and most importantly, a major frontier lies in understanding VMHvl function in the context of the broader meso-scale networks described here. Next-generation tools for simultaneously recording from and manipulating multiple brain regions simultaneously at cellular resolution, while integrating anatomic and transcriptomic information about different cell types within each region, offer an exciting opportunity to clarify the fine-grained system architecture within this overall circuitry, and may reveal a simplifying organizational logic to the seemingly daunting complexity described here.

Methods

All animal experiments were performed in accordance with NIH guidelines and approved by the California Institute of Technology Institutional Animal Care and Use Committee. For all injections, *Esr1*^{Cre} mice (8- to 12-wk-old, male and female) were anesthetized with isoflurane and mounted on a stereotaxic frame. For anterograde tracing, AAV1-FLEX-EGFP virus was injected by iontophoresis. Mice were killed 4 wk later and brains analyzed by TissueCyte 1000 serial two-photon tomography. For monosynaptic retrograde tracing, AAV1-DIO-TVA66T-dTom-N2cG (or AAV1-DIO-TVA66T-dTom for rabies glycoprotein-less control) virus was injected by iontophoresis into the VMHvl of *Esr1-Cre* male mice, followed by rabies EnvA-N2c-histone-GFP 3 wk later into the same location. Further details regarding rabies reagents are available on request from S.Y. and A.C. Mice were killed 9 d later and processed as above.

For subsequent experiments, serial sections were generated using a cryostat and images were acquired by confocal microscopy for starter cell images (Olympus FluoView FV1000), or by slide scanner for quantification of starter cell location and labeling outside of the VMHvl (Olympus VS-ASW-56). For the glutamatergic and GABAergic inputs study, HSV-LS1L-mCherry was injected into the VMHvl of vGLUT2-cre or vGAT-cre male mice. Mice were killed ~3 wk later. For poly-synaptic anterograde tracing, HSV1-H129ΔTK-TT viruses were injected into the VMHvl of *Esr1-Cre* males, and mice were killed 40–48 h later depending on health assessments. For the collateral projection study, HSV-LS1L-FLPo viruses were injected into projection targets of VMHvl^{Esr1} neurons in *Esr1-Cre* male mice. At the same time, FLP-dependent AAVDJ-fDIO-EYFP was injected into the VMHvl and mice were perfused 28–30 d later. For the projection-based input study, HSV-LS1L-FLPo was injected into the MPOA or PAG in *Esr1-Cre* male mice. At the same time, a 1:1 mixture of AAVDJ-fDIO-TVA and AAV8-fDIO-RG viruses were injected into the VMHvl, followed 3 wk later by rabies EnvA-ΔG-GFP. Mice were killed 6 d later. For dual-retrograde labeling, HSV-LS1L-mCherry and HSV-LS1L-EYFP was injected into the PAG and MPOA, respectively, in the same VMHvl^{Esr1} male mouse. Mice were killed ~3 wk later.

For quantification, images were analyzed using Fiji/ImageJ or Imaris Image Analysis Software (Bitplane, Oxford Instruments). Please see *SI Appendix, Supplemental Methods* for more detailed information.

ACKNOWLEDGMENTS. We thank Dr. Miquel Chillón Rodriguez, Dr. Fan Wang, Dr. Liqun Luo, and Dr. Rachael Neve for providing CAV-cre, retrograde Lenti-cre, TRIO reagents, and retrograde HSV-fDIO-cre viruses, respectively, for pilot experiments; Dr. Lynn Enquist and the Center for Neuroanatomy with Neurotropic Viruses viral core center (Princeton University) for H129 recombinants; Dr. Kimberly Ritola of Janelia Research Campus for G-deleted EnvA rabies viruses; Bin Yang for help with cell-volume measurement software; Ben Ouellette for technical help; C. Chiu for laboratory management; and G. Mancuso for administrative assistance. This work was supported by NIH Grants MH070053, MH085082, and MH112593 (to D.J.A.). B.W. is a Howard Hughes Medical Institute Fellow of the Life Sciences Research Foundation. D.J.A. is an Investigator of the Howard Hughes Medical Institute.

1. Sternson SM (2013) Hypothalamic survival circuits: Blueprints for purposive behaviors. *Neuron* 77:810–824.
2. Saper CB, Lowell BB (2014) The hypothalamus. *Curr Biol* 24:R1111–R1116.
3. Swanson LW (2005) Anatomy of the soul as reflected in the cerebral hemispheres: Neural circuits underlying voluntary control of basic motivated behaviors. *J Comp Neurol* 493:122–131.
4. Swanson LW (2000) Cerebral hemisphere regulation of motivated behavior. *Brain Res* 886:113–164.
5. Luiten PGM, ter Horst GJ, Steffens AB (1987) The hypothalamus, intrinsic connections and outflow pathways to the endocrine system in relation to the control of feeding and metabolism. *Prog Neurobiol* 28:1–54.
6. Hashikawa K, et al. (2017) *Esr1*⁺ cells in the ventromedial hypothalamus control female aggression. *Nat Neurosci* 20:1580–1590.
7. Lee H, et al. (2014) Scalable control of mounting and attack by *Esr1*⁺ neurons in the ventromedial hypothalamus. *Nature* 509:627–632.
8. Campbell JN, et al. (2017) A molecular census of arcuate hypothalamus and median eminence cell types. *Nat Neurosci* 20:484–496.
9. Correa SM, et al. (2015) An estrogen-responsive module in the ventromedial hypothalamus selectively drives sex-specific activity in females. *Cell Rep* 10:62–74.
10. Callaway EM (2008) Transneuronal circuit tracing with neurotropic viruses. *Curr Opin Neurobiol* 18:617–623.
11. Callaway EM, Luo L (2015) Monosynaptic circuit tracing with glycoprotein-deleted rabies viruses. *J Neurosci* 35:8979–8985.
12. Gielow MR, Zaborszky L (2017) The input-output relationship of the cholinergic basal forebrain. *Cell Rep* 18:1817–1830.
13. Hu R, Jin S, He X, Xu F, Hu J (2016) Whole-brain monosynaptic afferent inputs to basal forebrain cholinergic system. *Front Neuroanat* 10:98.
14. Li X, et al. (2018) Generation of a whole-brain atlas for the cholinergic system and mesoscopic projectome analysis of basal forebrain cholinergic neurons. *Proc Natl Acad Sci USA* 115:415–420.
15. Oh SW, et al. (2014) A mesoscale connectome of the mouse brain. *Nature* 508:207–214.
16. Schwarz LA, et al. (2015) Viral-genetic tracing of the input-output organization of a central noradrenergic circuit. *Nature* 524:88–92.
17. Wang D, et al. (2015) Whole-brain mapping of the direct inputs and axonal projections of POMC and AgRP neurons. *Front Neuroanat* 9:40.
18. Watabe-Uchida M, Zhu L, Ogawa SK, Vamanrao A, Uchida N (2012) Whole-brain mapping of direct inputs to midbrain dopamine neurons. *Neuron* 74:858–873.
19. Zhang Z, et al. (2017) Whole-brain mapping of the inputs and outputs of the medial part of the olfactory tubercle. *Front Neural Circuits* 11:52.
20. Andermann ML, Lowell BB (2017) Toward a wiring diagram understanding of appetite control. *Neuron* 95:757–778.
21. Atasoy D, Betley JN, Su HH, Sternson SM (2012) Deconstruction of a neural circuit for hunger. *Nature* 488:172–177.
22. Betley JN, Cao ZF, Ritola KD, Sternson SM (2013) Parallel, redundant circuit organization for homeostatic control of feeding behavior. *Cell* 155:1337–1350.
23. Wu Z, Autry AE, Bergan JF, Watabe-Uchida M, Dulac CG (2014) Galanin neurons in the medial preoptic area govern parental behaviour. *Nature* 509:325–330.
24. Kohl J, et al. (2018) Functional circuit architecture underlying parental behaviour. *Nature* 556:326–331.
25. Ishii KK, et al. (2017) A labeled-line neural circuit for pheromone-mediated sexual behaviors in mice. *Neuron* 95:123–137.e8.
26. Chen KS, et al. (2018) A hypothalamic switch for REM and non-REM sleep. *Neuron* 97:1168–1176.e4.
27. España RA, Reis KM, Valentino RJ, Berridge CW (2005) Organization of hypocretin/orexin efferents to locus coeruleus and basal forebrain arousal-related structures. *J Comp Neurol* 481:160–178.
28. Wang L, Chen IZ, Lin D (2015) Collateral pathways from the ventromedial hypothalamus mediate defensive behaviors. *Neuron* 85:1344–1358.
29. Lee EY, Lee HS (2016) Dual projections of single orexin- or CART-immunoreactive, lateral hypothalamic neurons to the paraventricular thalamic nucleus and nucleus accumbens shell in the rat: Light microscopic study. *Brain Res* 1634:104–118.
30. Ren J, et al. (2018) Anatomically defined and functionally distinct dorsal raphe serotonin sub-systems. *Cell* 175:472–487.e20.
31. Akesson TR, Ulibarri C, Truitt S (1994) Divergent axon collaterals originate in the estrogen receptive ventromedial nucleus of hypothalamus in the rat. *J Neurobiol* 25:406–414.
32. Yang CF, et al. (2013) Sexually dimorphic neurons in the ventromedial hypothalamus govern mating in both sexes and aggression in males. *Cell* 153:896–909.
33. Anderson DJ (2016) Circuit modules linking internal states and social behaviour in flies and mice. *Nat Rev Neurosci* 17:692–704.
34. Bayless DW, Shah NM (2016) Genetic dissection of neural circuits underlying sexually dimorphic social behaviours. *Philos Trans R Soc Lond B Biol Sci* 371:20150109.
35. Chen P, Hong W (2018) Neural circuit mechanisms of social behavior. *Neuron* 98:16–30.
36. Hashikawa Y, Hashikawa K, Falkner AL, Lin D (2017) Ventromedial hypothalamus and the generation of aggression. *Front Syst Neurosci* 11:94.
37. Kennedy A, et al. (2014) Internal states and behavioral decision-making: Toward an integration of emotion and cognition. *Cold Spring Harb Symp Quant Biol* 79:199–210.
38. Yang CF, Shah NM (2014) Representing sex in the brain, one module at a time. *Neuron* 82:261–278.
39. Choi GB, et al. (2005) *Lhx6* delineates a pathway mediating innate reproductive behaviors from the amygdala to the hypothalamus. *Neuron* 46:647–660.
40. Roeling TAP, et al. (1994) Efferent connections of the hypothalamic “aggression area” in the rat. *Neuroscience* 59:1001–1024.
41. Toth M, Fuzesi T, Halasz J, Tulogdi A, Haller J (2010) Neural inputs of the hypothalamic “aggression area” in the rat. *Behav Brain Res* 215:7–20.
42. Canteras NS, Simerly RB, Swanson LW (1994) Organization of projections from the ventromedial nucleus of the hypothalamus: A *Phaseolus vulgaris*-leucoagglutinin study in the rat. *J Comp Neurol* 348:41–79.
43. Morrell JI, Pfaff DW (1982) Characterization of estrogen-concentrating hypothalamic neurons by their axonal projections. *Science* 217:1273–1276.
44. Saper CB, Swanson LW, Cowan WM (1976) The efferent connections of the ventromedial nucleus of the hypothalamus of the rat. *J Comp Neurol* 169:409–442.
45. Fahrbach SE, Morrell JI, Pfaff DW (1989) Studies of ventromedial hypothalamic afferents in the rat using three methods of HRP application. *Exp Brain Res* 77:221–233.
46. Turcotte JC, Blaustein JD (1999) Projections of the estrogen receptor-immunoreactive ventrolateral hypothalamus to other estrogen receptor-immunoreactive sites in female guinea pig brain. *Neuroendocrinology* 69:63–76.
47. Chi CC (1970) Afferent connections to the ventromedial nucleus of the hypothalamus in the rat. *Brain Res* 17:439–445.
48. Ter Horst GJ, Luiten PGM (1987) *Phaseolus vulgaris* leuco-agglutinin tracing of intrahypothalamic connections of the lateral, ventromedial, dorsomedial and paraventricular hypothalamic nuclei in the rat. *Brain Res Bull* 18:191–203.
49. Shimogawa Y, Sakuma Y, Yamanouchi K (2015) Efferent and afferent connections of the ventromedial hypothalamic nucleus determined by neural tracer analysis: Implications for lordosis regulation in female rats. *Neurosci Res* 91:19–33.
50. Sakurai K, et al. (2016) Capturing and manipulating activated neuronal ensembles with CANE delineates a hypothalamic social-fear circuit. *Neuron* 92:739–753.
51. Ragan T, et al. (2012) Serial two-photon tomography for automated ex vivo mouse brain imaging. *Nat Methods* 9:255–258.
52. Wickersham IR, Finke S, Conzelmann KK, Callaway EM (2007) Retrograde neuronal tracing with a deletion-mutant rabies virus. *Nat Methods* 4:47–49.
53. Wickersham IR, et al. (2007) Monosynaptic restriction of transsynaptic tracing from single, genetically targeted neurons. *Neuron* 53:639–647.
54. Ugolini G (1995) Specificity of rabies virus as a transneuronal tracer of motor networks: Transfer from hypoglossal motoneurons to connected second-order and higher order central nervous system cell groups. *J Comp Neurol* 356:457–480.
55. Lo L, Anderson DJ (2011) A Cre-dependent, anterograde transsynaptic viral tracer for mapping output pathways of genetically marked neurons. *Neuron* 72:938–950.
56. Anthony TE, et al. (2014) Control of stress-induced persistent anxiety by an extra-amygdala septohypothalamic circuit. *Cell* 156:522–536.
57. Wojaczynski GJ, Engel EA, Steren KE, Enquist LW, Patrick Card J (2015) The neuroinvasive profiles of H129 (herpes simplex virus type 1) recombinants with putative anterograde-only transneuronal spread properties. *Brain Struct Funct* 220:1395–1420.
58. Todd WD, et al. (2018) A hypothalamic circuit for the circadian control of aggression. *Nat Neurosci* 21:717–724.
59. Sakuma Y, Tada K (1984) Evidence that two sizes of ventromedial hypothalamic neurons project to the mesencephalic central grey matter in rats. *J Physiol* 349:287–297.
60. Sakuma Y, Akaiishi T (1987) Cell size, projection path, and localization of estrogen-sensitive neurons in the rat ventromedial hypothalamus. *J Neurophysiol* 57:1148–1159.
61. Millhouse OE (1973) The organization of the ventromedial hypothalamic nucleus. *Brain Res* 55:71–87.
62. Ciriello J, McMurray JC, Babic T, de Oliveira CVR (2003) Collateral axonal projections from hypothalamic hypocretin neurons to cardiovascular sites in nucleus ambiguus and nucleus tractus solitarius. *Brain Res* 991:133–141.
63. Yoon YS, Lee HS (2013) Projection patterns of lateral hypothalamic, cocaine- and amphetamine-regulated transcript (CART) neurons to the dorsal raphe and/or the locus coeruleus in the rat. *Brain Res* 1494:56–69.
64. Vertes RP, McKenna JT (2000) Collateral projections from the supramammillary nucleus to the medial septum and hippocampus. *Synapse* 38:281–293.
65. Luo SX, et al. (2018) Regulation of feeding by somatostatin neurons in the tuberal nucleus. *Science* 361:76–81.
66. Kecsichull JM, et al. (2016) High-throughput mapping of single-neuron projections by sequencing of barcoded RNA. *Neuron* 91:975–987.
67. Millhouse OE (1973) Certain ventromedial hypothalamic afferents. *Brain Res* 55:89–105.